energies

Article

Magnetic Equivalent Circuit and Optimization Method of a Synchronous Reluctance Motor with Concentrated Windings

Gan Zhang [1,*], Jinxin Tao [1], Yifan Li [1], Wei Hua [1], Xiaohan Xu [2] and Zhihong Chen [3]

[1] School of Electrical Engineering, Southeast University, Nanjing 210096, China; 17851950582@163.com (J.T.); 15850656599@163.com (Y.L.); huawei1978@seu.edu.cn (W.H.)
[2] State Grid Jiangsu Electric Power Co., Ltd. Maintenance Branch Company, Nanjing 211102, China; xxh-hayley@foxmail.com
[3] Beijing Institute of Precision Mechatronics and Controls, Beijing 100076, China; zhihongch@outlook.com
* Correspondence: zhanggan@seu.edu.cn; Tel.: +86-1570-518-1487

Abstract: In this paper, the 12-slot/4-pole (12/4) synchronous reluctance motor (SynRM) with concentrated windings is proposed for low-cost hybrid vehicles. The non-linear magnetic equivalent circuit (MEC) model of the 12/4 SynRM is built to obtain the main electromagnetic characteristics such as coil flux, inductances, torque, etc. The magnetic saturation is also counted in by the MEC. Results calculated by MEC are validated by 2D finite element analysis (FEA). Then, aiming at larger average torque, lower torque ripple and lower total harmonic distortion (THD) in phase voltage, the parameter optimization method of the SynRM is proposed based on the Taguchi method and the MEC model. The proposed Taguchi-MEC method enables a fast optimization with satisfactory accuracy. Finally, the motor prototype is manufactured, and experimental validations are carried out.

Keywords: magnetic circuit; optimization; synchronous reluctance; torque performances

check for updates

Citation: Zhang, G.; Tao, J.; Li, Y.; Hua, W.; Xu, X.; Chen, Z. Magnetic Equivalent Circuit and Optimization Method of a Synchronous Reluctance Motor with Concentrated Windings. *Energies* **2022**, *15*, 1735. https://doi.org/10.3390/en15051735

Academic Editor: Mario Marchesoni

Received: 18 January 2022
Accepted: 23 February 2022
Published: 25 February 2022

1. Introduction

Thanks to the simple structure and robust rotor without a brush and slip ring, the synchronous reluctance motor (SynRM) has become an attractive candidate [1–3]. Conventional SynRMs employ distributed windings to obtain essentially sinusoidal back electromotive force (back-EMF) per phase and a high winding factor [4–7]. However, due to the long end-part winding length, distributed windings result in increased copper loss, decreased efficiency and power density. On the other hand, concentrated windings are rarely employed for SynRMs because of the high harmonic distortion in armature windings and low winding factor. Spargo and other authors introduce fractional slot concentrated windings (FSCW) to SynRM, with a segment stator to improve torque density and efficiency [8–14], e.g., the 6-slot 4-pole (6/4) SynRel machine. The 6/4 machine exhibits a comparable performance of a permanent magnet (PM)-assisted SynRM with a high torque output capability and a low level of torque ripple [8,9]. The proposed 12/4 CW machine exhibits comparable torque performance, compared to the case of adopting distributed winding, when the total stack length is unchanged. The short winding end, PM-free and very low mutual inductances of the 12/4 CW machine will be appreciated by applications where a short stack length, high robustness and low cost are required, such as the integrated starter generator (ISG) in low-cost wild hybrid vehicles. The ISG is located between the engine and the gear box, and drives the output shaft directly. First of all, the vehicle producer requires a brushless and PM-less motor and concentrated windings. Getting rid of permanent magnets reduces the cost and enhances robustness and speed range. Avoiding distributed windings improves the air flow and makes it more dustproof, as well as other mechanical considerations. These above requirements leave only the choices of the reluctance motor and SynRM. The 9/6 or 15/8 SynRM are not considered due to unbalanced radial forces on the rotor. More importantly, low mutual inductances between armature phases is highly appreciated, since it will facilitate a high fault-tolerant capability, which can be found in the 12/4 SynRM machine.

Consequently, the magnetic equivalent circuit (MEC) model is built to predict electromagnetic performance, including air-gap flux density distributions, winding inductances and electromagnetic torque. Then, the obtained results are validated by 2D-finite element analysis (2D-FEA). Furthermore, aiming at better torque performances and lower total harmonic distortion (THD) in phase voltage, the optimization of the 12/4 SynRM is carried out combing the MEC and Taguchi method. Unlike traditional optimization methods using FEA coupling optimization algorithms, such as a genetic algorithm [15–18] and particle swarm algorithm [19–22], the Taguchi method exhibits the merit of being less time consuming [23–26]. This merit can be greatly enhanced by using MEC instead of FEA, maintaining satisfactory accuracy.

2. Machine Topologies and Design Specifications

This section provides a brief introduction to a prototype of the 12/4 SynRM. The topology structure of the designed 12/4 SynRM is shown in Figure 1, with the key dimensional parameters listed in Table 1. The outer dimensions of the stator are chosen based on the available test bench and power converters for the following experiment. The segmented stator core is designed to improve the slot filling factor (SFF). Torque ripple reduction also needs to be mitigated, so that a continuous skew rotor is adopted. It should be noted that the skewing angle is optimized to achieve a balance between the sinusoidal back-EMF and electromagnetic torque. Two rotors are manufactured, one without skewing and another with skewing. This paper only introduces the 12/4 SynRM without rotor skewing. The skewed rotor will be introduced in another coming paper. Moreover, the seam/gap between the neighboring stator segments depends on the manufacturing accuracy and are normally less than 0.05 mm. Considering these seams are very small, their influences on magnetic performances can be neglected and not considered in the MEC and FEA models.

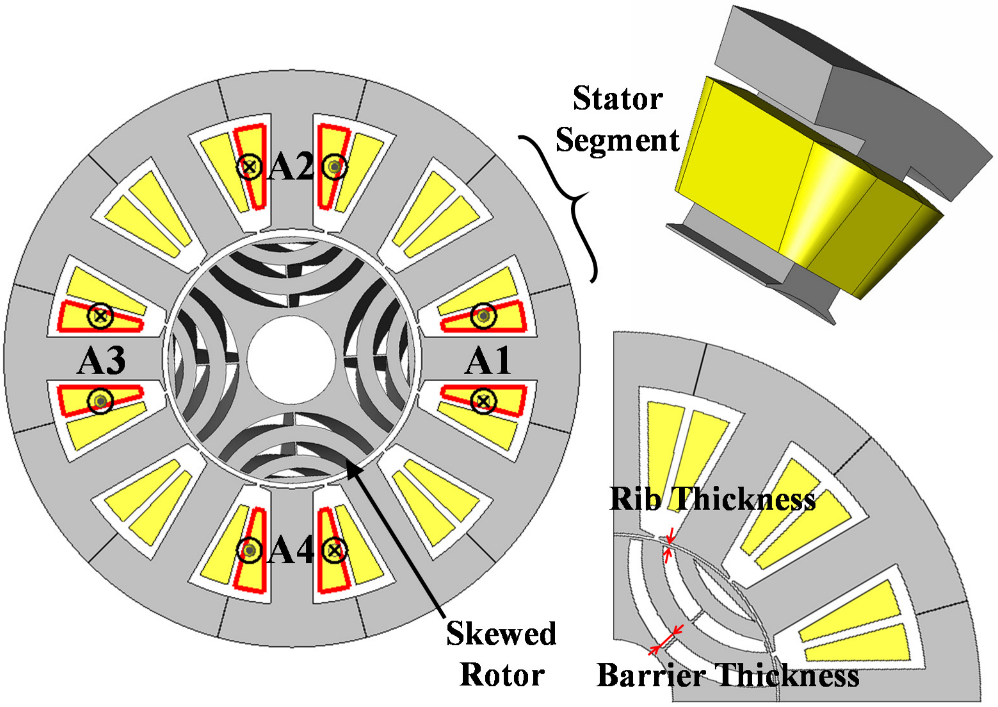

Figure 1. Topology of the 12/4 SynRM with concentrated windings with stator module and a quarter part.

Table 1. Main Design Specifications of the 12/4 Machine.

Item	Value
Outer diameter	150 mm
Lamination length	75 mm
Total end winding	20 mm
Total stack length	95 mm
β_2	12.4°
w_{b1}	10.00 mm
s_{tooth}	11.12 mm
s_{yoke}	11.38 mm
β_1	11.10°
d_{m1}	4.41 mm
$w_{rib1\text{-}1}$	0.58 mm
w_{rib2}	0.28 mm
d_{m2}	3.50 mm
$w_{rib1\text{-}2}$	0.50 mm
l_{so}	1.0 mm
Turns per coil	30
Copper fill factor	0.58
d-axis inductance (FEA)	19.3 mH
q-axis inductance (FEA)	6.2 mH
Phase current	30.1 A
Current angle	55°

3. Magnetic Equivalent Circuit Method and Evaluation

As an efficient tool, the MEC method has been widely utilized to analyze the electromagnetic performance of electrical machines [27,28], and is considered as a compromise between FEA with high accuracy and an analytical method (AM) with straightforward physical connections of performance and geometrical parameters. Therefore, the MEC model of the 12/4 SynRM is built in this paper. Figure 2 illustrates a quarter of the 12/4 machine, where each specific magnetic path is illustrated by a different MEC branch. The SynRM is separated into segments according to the geometrical shape. The equivalent permeance of each part of the stator and rotor core can be calculated using the permeance equations.

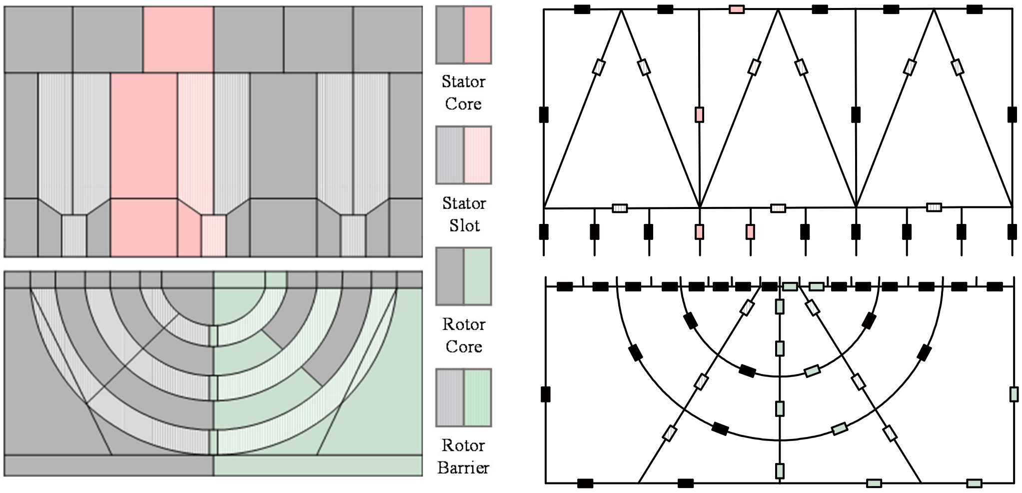

(**a**) (**b**)

Figure 2. MEC model for a quarter of 12/4 SynRM. (**a**) 1/4 topology, (**b**) 1/4 MEC model.

The basic equation which governs each branch of the magnetic circuit is given by,

$$\frac{\Phi}{G} = F \tag{1}$$

$$G = \mu_i \mu_0 \frac{S}{l} \tag{2}$$

In Equation (1), Φ, G and F are the flux, permeance and magnetic-motive-force (MMF), respectively. In Equation (2), μ_r, μ_0, S and l are the relative permeability, the permeability of free space, the cross-section area and the length, respectively. Specifically, μ_r is determined by iteration from the B–H curve of the lamination material. The permanent magnets can simply be modeled as an equivalent MMF [29],

$$F_m = \frac{B_r}{\mu_i \mu_0} h_m \tag{3}$$

and permeance,

$$G_m = \mu_i \mu_0 \frac{l_m l_a}{h_m} \tag{4}$$

where h_m and l_m are the magnet thickness and width, respectively, and B_r is the remanence.

Then, the MEC model is solved by MATLAB following the flow chart shown in Figure 3. The saturation in iron is counted in by the iteration of μ_r. For each branch in the magnetic circuit at the ith step in an iteration, the condition of convergence ε is defined as,

$$\varepsilon = \left| \frac{\mu_i - \mu_i'}{\mu_i} \right| \leq 10^{-6} \tag{5}$$

where μ_i is the permeance given before equation solving, and μ'_i is the real permeance obtained after the equation solving, as shown in Figure 4. If $\varepsilon \leq 10^{-6}$ is not achieved, the permeance at the $(i + 1)$th step in an iteration is given by Equation (6) and $k = 0.5$ in this case.

$$\mu_{i+1} = (1-k)\mu_i + k\mu_i', \; 0 < k < 1 \tag{6}$$

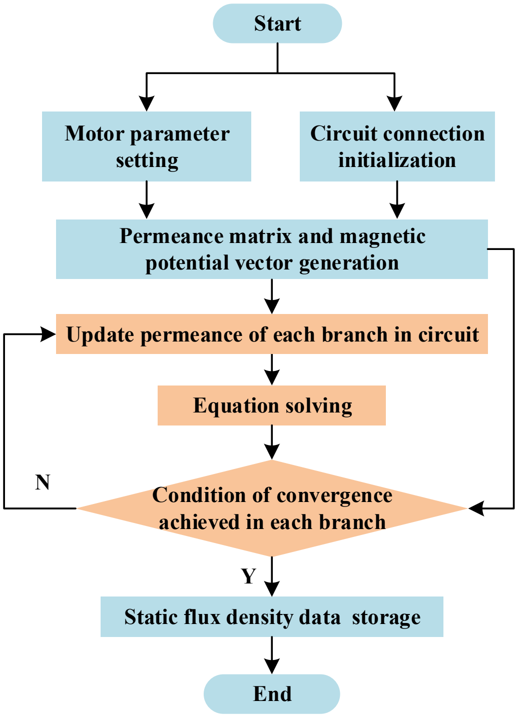

Figure 3. Calculation flow chart of the MEC model at each rotor position.

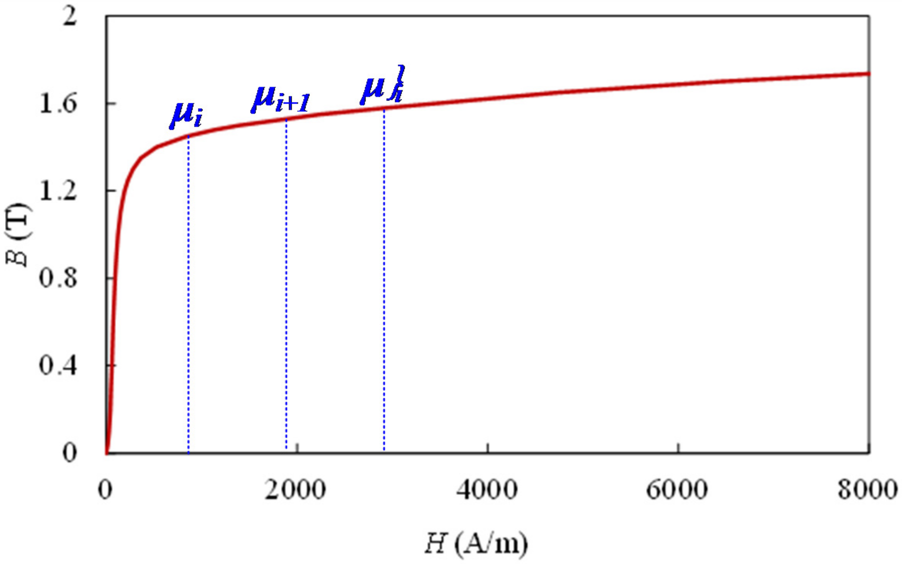

Figure 4. Demonstration of the convergence process according to the B–H curve.

Figure 5 shows the mesh results of the FEA model in which the air-gap consists of 6 layers of elements. The path to plot the air-gap flux density distribution is also given in Figure 5a, which covers 1/4 of the air-gap. The air-gap flux density distributions generated by phase-A current, d-axis current and q-axis current, respectively, are predicted by MEC and then compared to the FEA results by Figure 6. Overall, satisfied agreements are achieved.

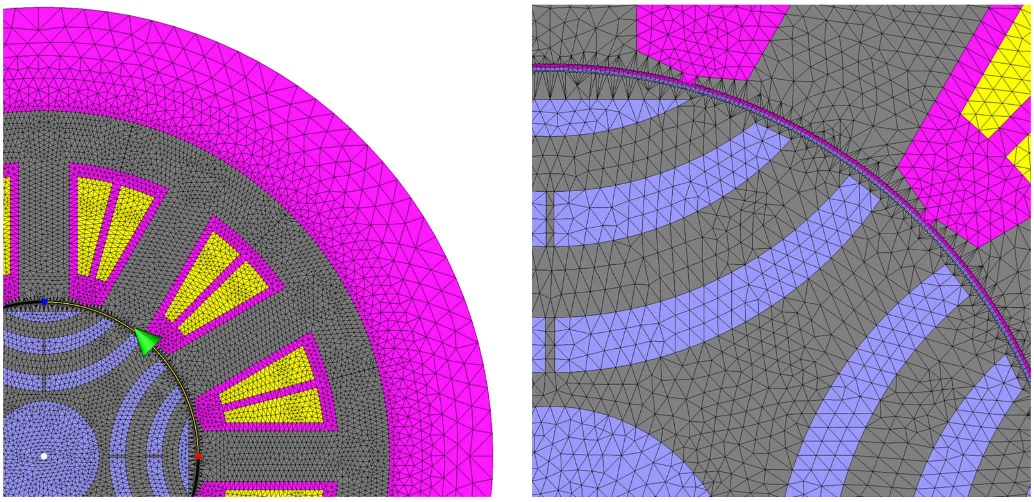

(**a**) (**b**)

Figure 5. Elements in the FEA mesh. (**a**) The path to plot air-gap flux density, (**b**) mesh details.

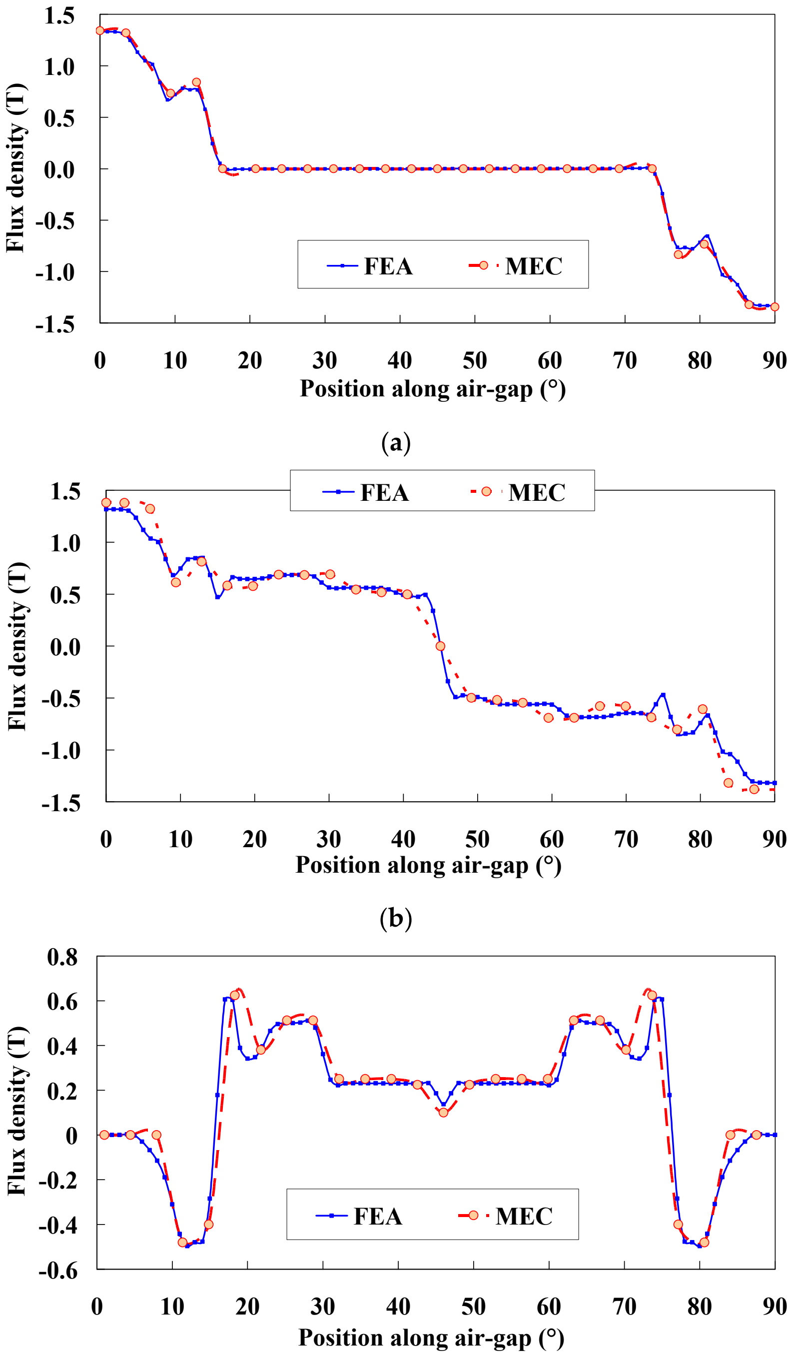

(**a**)

(**b**)

(**c**)

Figure 6. Air-gap flux density distributions: (**a**) by phase-A current; (**b**) by d-axis current; (**c**) by q-axis current.

4. Results and Discussion

When the MEC model of the 12/4 SynRM motor is solved, the electromagnetic characteristics can be easily calculated, e.g., the flux in the air-gap (Φ_A), coil flux linkage (Ψ_a), phase-A self-inductance (L_{aa}) and mutual inductance between phase-A and -B (M_{ba}) can be obtained by

$$\Phi_A = \int BdS \tag{7}$$

$$\Psi_A = N(\Phi_A + \Phi_{\delta A}) \tag{8}$$

$$L_{aa} = \frac{\Psi_A}{I_A} \tag{9}$$

$$M_{ba} = \frac{\Psi_B}{I_A} \tag{10}$$

Then, the L_d (d-axis), L_q (q-axis) and L_{dq} (d-q coupled inductance) can be calculated by Equations (11) and (12). Figure 7 compares the MEC and FEA obtained inductances with good agreements.

$$\begin{bmatrix} L_d \\ L_q \\ L_{dq} \end{bmatrix} = P \begin{bmatrix} L_{aa} & M_{ba} & M_{ca} \\ M_{ab} & L_{bb} & M_{cb} \\ M_{ac} & M_{bc} & L_{cc} \end{bmatrix} P^{-1} \tag{11}$$

$$P = \frac{2}{3} \begin{bmatrix} \cos\theta & \cos\left(\theta - \frac{2}{3}\pi\right) & \cos\left(\theta + \frac{2}{3}\pi\right) \\ -\sin\theta & -\sin\left(\theta - \frac{2}{3}\pi\right) & -\sin\left(\theta + \frac{2}{3}\pi\right) \\ \frac{1}{2} & \frac{1}{2} & \frac{1}{2} \end{bmatrix} \tag{12}$$

$$P^{-1} = \begin{bmatrix} \cos\theta & -\sin\theta & \frac{1}{2} \\ \cos\left(\theta - \frac{2}{3}\pi\right) & -\sin\left(\theta - \frac{2}{3}\pi\right) & \frac{1}{2} \\ \cos\left(\theta + \frac{2}{3}\pi\right) & -\sin\left(\theta + \frac{2}{3}\pi\right) & \frac{1}{2} \end{bmatrix} \tag{13}$$

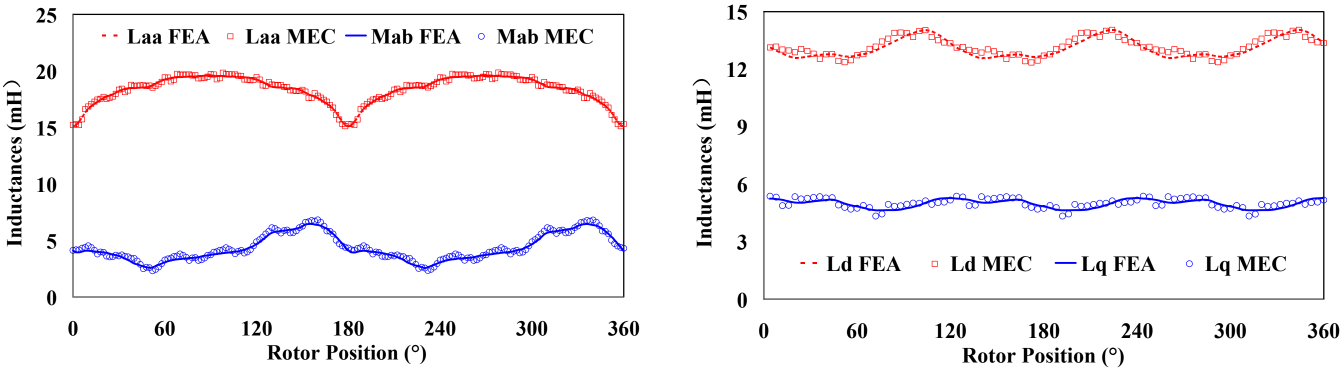

(**a**) (**b**)

Figure 7. Comparison of the inductance results obtained by MEC and FEA. (**a**) Phase self and mutual inductances when 1 A is applied in phase-A. (**b**) d-axis and q-axis inductances at rated operation.

It should be noted that in the 12/4 SynRM with concentrated windings, there is a cross-coupling between the d-axis and q-axis, i.e., the L_{dq} contributes unneglectable electromagnetic torque, as given in Equation (14).

$$T = \frac{3}{2} p {i_s}^2 \left[\frac{1}{2} \left(L_d - L_q \right) \sin 2\alpha + L_{dq} \cos 2\alpha \right] \tag{14}$$

where p is the rotor pole-pairs, L_d and L_q is the d- and q-axis inductance, respectively, and α is the current phase angle, i.e., the angle between the current vector and d-axis. Thus, the torque waveform can be calculated. Figures 8 and 9 give the torque performance versus current phases and rotor position, respectively. As can be seen, good agreements are achieved between the MEC and FEA results.

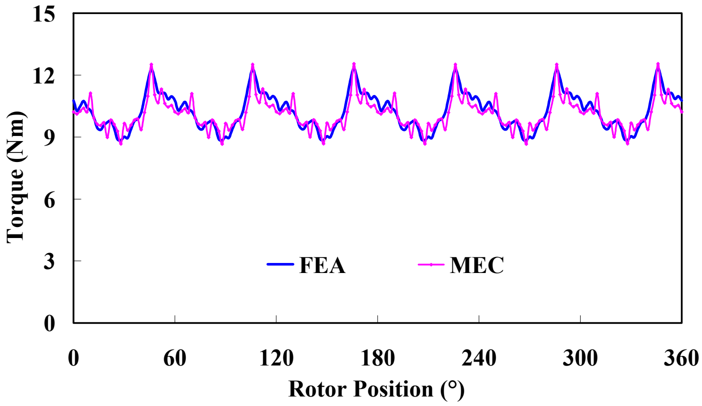

Figure 8. Torque vs. rotor positions when 30 A is applied.

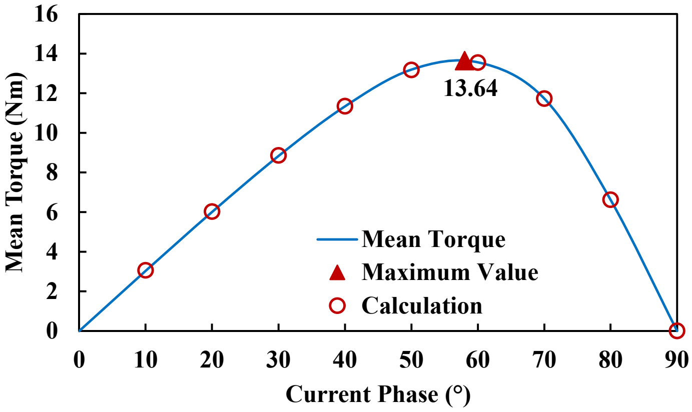

Figure 9. Average torque, calculation values vs. current phases when 50 A is applied.

5. Optimization of Torque Characters Based on MEC and Taguchi Method

The Taguchi method is chosen as one of the many optimization methods. The optimization methods introduced in Section 1 require sophisticated algorithms and additional programming and data processing along with a lot of FEA cases of electromagnetic field. So, the methods are usually time consuming and complex. On the other hand, the Taguchi method can obtain satisfactory results by reduced calculation cases, and thus is less time consuming. In this paper, the Taguchi method and the MEC model are used to optimize the SynRM. The steps in the Taguchi method are as follows [30]:

1. Select the parameters and determine its levels.
2. Design of exams.
3. Review the optimization results.

First of all, the means of all results $M_t(S)$ and average effect M_{Xj} can be calculated as

$$M_t(S) = \frac{1}{n}\sum_{p_n=1}^{n} S_{p_n} \tag{15}$$

$$M_{X_j}(Y) = \frac{1}{3}(Y_1 + Y_2 + Y_3) \tag{16}$$

where X_i and Y_i are factor-level and performances, respectively. Then, the analysis of variance is carried out, which provides a measure of confidence. The technique does not directly analyze the data, but rather determines the variance of the data. The sum of squares

(SS) is calculated first. It is a measure of the deviation of the experimental data from the mean value of the data. The sum of squares due to various factors can be calculated as

$$SS = j \sum_{p_j=1}^{j} \left(M_{X_{p_j}}(Y) - M_t(S) \right)^2 \tag{17}$$

where $M_t(S)$ and $M_{xpj}(Y)$ are results of Equations (5) and (6). SS shows the relative importance of various factors on machine performance. Then, the Pearson coefficient is chosen to calculate the coefficient of correlation and given as

$$\rho_{X_i,Y_i} = \frac{n \sum X_i Y_i - \sum X_i \sum Y_i}{\sqrt{n \sum X_i^2 - \left(\sum X_i\right)^2} \sqrt{n \sum Y_i^2 - \left(\sum Y_i\right)^2}} \tag{18}$$

The optimization aim is a larger average torque (T_{avg}), lower torque ripple (T_{rip}) and lower THD of phase voltage (THD_U). Firstly, the optimization parameters are determined and shown in Figure 10 and listed in Table 2, which are related to the rotor barriers and ribs, stator tooth and yoke width.

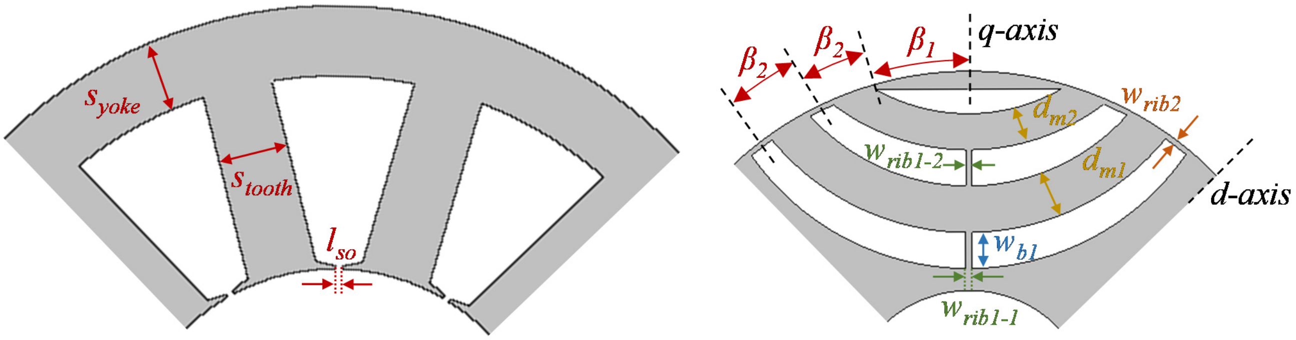

(**a**) (**b**)

Figure 10. Design parameters to be optimized. (**a**) Stator part. (**b**) Rotor part.

Table 2. Design Parameters and Their Variation Levels.

Parameter	Level 1	Level 2	Level 3
β_1	11.5°	12.5°	12°
β_2	11.5°	12.5°	12°
d_{m1}	3.5 mm	4.5 mm	4 mm
d_{m2}	2.5 mm	3.5 mm	3 mm
w_{b1}	3 mm	4 mm	3.5 mm
w_{rib1}	0.55 mm	0.65 mm	0.6 mm
w_{rib2}	0.45 mm	0.55 mm	0.5 mm
s_{yoke}	10 mm	12 mm	11 mm
s_{tooth}	10 mm	12 mm	11 mm
l_{so}	0.8 mm	1.2 mm	1 mm

The design of the exam is carried out after preparing the initial information. To obtain the number of exams, the orthogonal arrays are presented using Taguchi. The exams' matrix can be easily created using existing software, in this case the Minitab. Shown in Table 3 are the Taguchi experiments that are tailored to their parameters and levels. The rows of the exams table represent the levels of factors in each experiment, and its columns represent the number of factors.

Table 3. Exams Table.

Exams	A	B	C	D	E	F	G	H	J	K
1	1	1	1	1	1	1	1	1	1	1
2	1	1	1	1	2	2	2	2	2	2
3	1	1	1	1	3	3	3	3	3	3
4	1	2	2	2	1	1	1	2	2	2
5	1	2	2	2	2	2	2	3	3	3
6	1	2	2	2	3	3	3	1	1	1
7	1	3	3	3	1	1	1	3	3	3
8	1	3	3	3	2	2	2	1	1	1
9	1	3	3	3	3	3	3	2	2	2
10	2	1	2	3	1	2	3	1	2	3
11	2	1	2	3	2	3	1	2	3	1
12	2	1	2	3	3	1	2	3	1	2
13	2	2	3	1	1	2	3	2	3	1
14	2	2	3	1	2	3	1	3	1	2
15	2	2	3	1	3	1	2	1	2	3
16	2	3	1	2	1	2	3	3	1	2
17	2	3	1	2	2	3	1	1	2	3
18	2	3	1	2	3	1	2	2	3	1
19	3	1	3	2	1	3	2	1	3	2
20	3	1	3	2	2	1	3	2	1	3
21	3	1	3	2	3	2	1	3	2	1
22	3	2	1	3	1	3	2	2	1	3
23	3	2	1	3	2	1	3	3	2	1
24	3	2	1	3	3	2	1	1	3	2
25	3	3	2	1	1	3	2	3	2	1
26	3	3	2	1	2	1	3	1	3	2
27	3	3	2	1	3	2	1	2	1	3

Using the results of experiments designed using the Taguchi method and after analyzing the results of the experiments, the optimal combination of factor levels and output voltage and cost values are calculated at the optimal point. The effect of each level is listed in Table 4.

Table 4. The Average Value of Levels.

Value	**T_{avg} (Nm)**			**T_{rip}**			**THD_U**		
Level	**1**	**2**	**3**	**1**	**2**	**3**	**1**	**2**	**3**
β_1	9.80	9.82	9.79	0.43	0.41	0.41	0.41	0.37	0.39
β_2	9.57	9.97	9.82	0.55	0.32	0.35	0.39	0.38	0.39
d_{m1}	10.12	9.80	9.77	0.34	0.44	0.44	0.39	0.38	0.39
d_{m2}	9.72	9.68	9.85	0.41	0.43	0.43	0.39	0.38	0.39
w_{b1}	9.26	10.13	9.61	0.42	0.43	0.44	0.39	0.37	0.39
w_{rib1}	9.64	9.99	9.73	0.38	0.41	0.39	0.35	0.42	0.36
w_{rib2}	9.93	9.85	9.81	0.43	0.43	0.42	0.38	0.39	0.38
s_{yoke}	9.98	9.42	9.86	0.42	0.42	0.41	0.39	0.38	0.39
s_{tooth}	9.58	9.99	9.87	0.43	0.41	0.44	0.41	0.36	0.38
l_{so}	9.82	9.88	9.83	0.41	0.45	0.43	0.38	0.38	0.38

Figures 11–13 present the output graph for different levels of each parameter. It can be observed that T_{avg} is most sensitive to S_{yoke} and S_{tooth}, while T_{rip} is most sensitive to β_2, w_{b1} and S_{tooth}. On the other hand, w_{b1} and S_{tooth} have the greatest influence on THD_U.

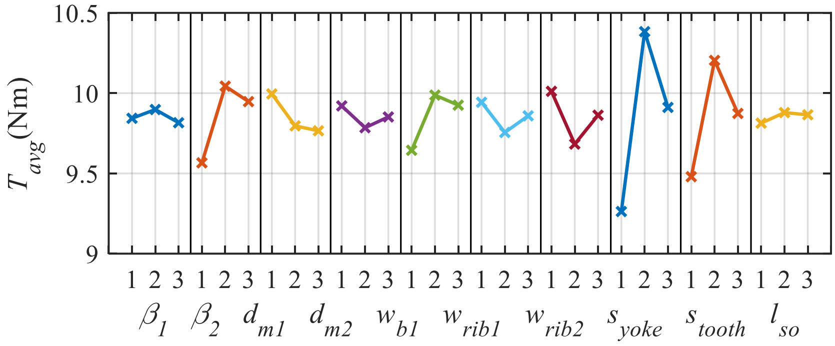

Figure 11. Plot of main factor effects on average torque (T_{avg}).

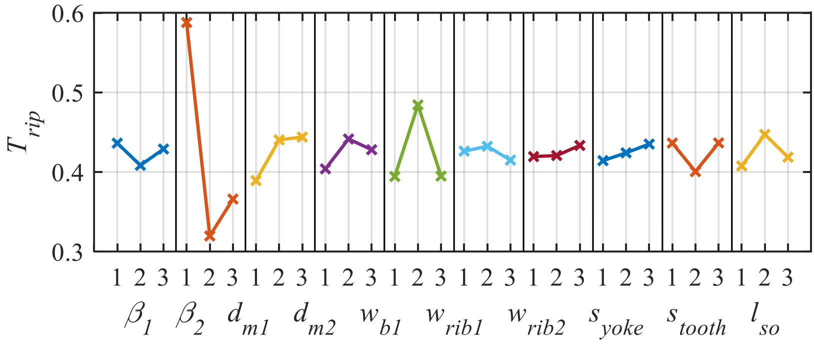

Figure 12. Plot of main factor effects on torque ripple (T_{rip}).

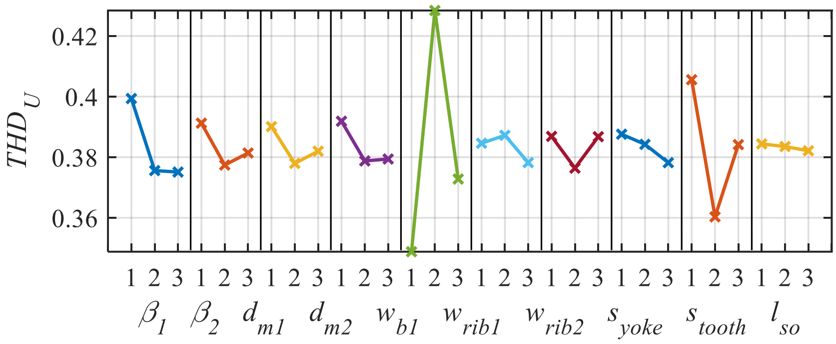

Figure 13. Plot of main factor effects on THD of phase voltage (THD_U).

Table 5 gives the initial parameters and Taguchi-MEC optimized parameters. Table 6 compares the T_{avg}, T_{rip} and THD_U. As can be seen, the final results obtained by Taguchi-MEC are very close to those obtained by the multi-object optimization carried out on JMAG. It should be emphasized that the total time needed for Taguchi-MEC is 10 min (including nearly 8 min organizing data), while the time needed for JMAG is nearly 58 h (43,086 elements in mesh and 180 steps in each case). Overall, the proposed Taguchi-MEC method exhibits the great advantage of fast calculation with promising accuracy.

A brief comparison of the proposed 12/4 SynRM with existing state of the art is carried out. Figure 14 shows the 12/4 SynRM with concentrated winding (CW) and its counterpart, i.e., the 12/4 SynRM with distributed windings (DW). As can be seen, the end winding in the CW machine is much smaller than the DW one; thus, more laminations can be adopted when the same stack length is achieved. A higher copper fill factor and more coil turns are also obtained by the CW machine. More details regarding design specification and electromagnetic performances are given in Table 7, where the DW SynRM is optimized by a multi-object optimization method carried out on JMAG. The fault tolerant capability is evaluated by the mutual linkage coefficient k_{ml}, which is also given in Table 7.

Table 5. Comparison of the Parameters and Performances.

Parameters	Initial	Optimized by Taguchi-MEC
β_2	12.0°	12.4°
w_{b1}	3.50 mm	10.00 mm
s_{tooth}	11.00 mm	11.12 mm
s_{yoke}	11.00 mm	11.38 mm
β_1	12.00°	11.10°
d_{m1}	3.50 mm	4.41 mm
$w_{rib1\text{-}1}$	0.60 mm	0.58 mm
w_{rib2}	0.50 mm	0.28 mm
d_{m2}	2.50 mm	3.50 mm
$w_{rib1\text{-}2}$	0.60 mm	0.50 mm
l_{so}	1.0 mm	1.0 mm

Table 6. Comparison of the Optimization Results Between Taguchi-MEC and FEA.

Results	Initial	Taguchi-MEC	FEA (by JMAG)
T_{avg}	9.40 Nm	9.82 Nm	9.90 Nm
T_{rip}	37.4%	31.2%	30.5%
THD_U	37%	35%	35%

$$k_{ml} = \frac{\sum_{\theta=0}^{360}(|M_{ab}|)}{\sum_{\theta=0}^{360}(L_{aa})} \tag{19}$$

where θ is electrical rotor position. The smaller k_{ml} indicates weaker mutual linkage between armature phases and thus better fault tolerant capability. As can be seen from Table 7, the proposed 12/4 CW SynRM shows a better torque output result and much better k_{ml} than the traditional 12/4 DW SynRM. The advantage of the torque performances of the CW machine is more obvious when the total stack length is smaller than 95 mm since the proportion of lamination length to total stack length varies with available space in stack.

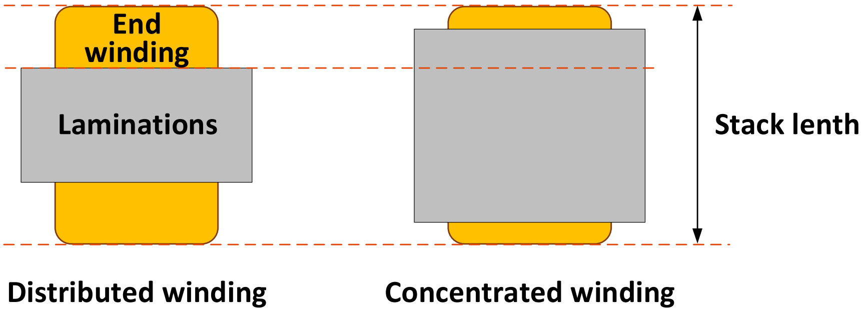

Figure 14. Demonstration of the end winding of the 12/4 SynRMs.

Table 7. Design Specifications of the 12/4 SynRMs.

Item	Distributed Winding	Concentrated Winding
Outer diameter	150 mm	150 mm
Lamination length	50 mm	75 mm
Total end winding	45 mm	20 mm
Total stack length	95 mm	95 mm
Turns per coil	30	40
Copper fill factor	0.5	0.58
Average torque	9.6 Nm	9.9 Nm
Torque ripple	30%	30.5%
Mutual linkage coefficient, k_{ml}	50%	14%

6. Experimental Validation

The experimental setup shown in Figure 15 consists of a prototyped 12/4 SynRM and a back-to-back load machine, which are both controlled by inverters. The load machine of the experimental platform supports the torque range of 50 Nm and the max speed of 15,000 r/min. The inverter supports the power of 30 kW/60 A. The torque sensor supports the torque range of 50 Nm/10 Nm with the accuracy of 0.1%, respectively. The torque shown in Figure 16 is measured by a sensor positioned between the SynRM and the load machine. Figure 17 compares the torque values obtained by MEC and FEA, and as can be seen, good agreements are achieved. The FEA calculated losses and efficiency is given in Table 8, and the measured efficiency under different rotor speed is presented in Figure 18.

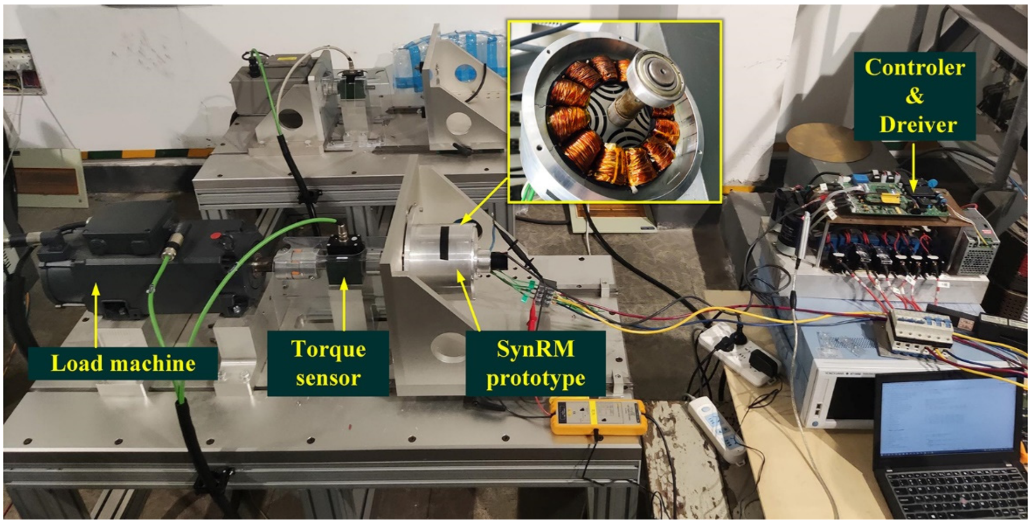

Figure 15. Experimental platform.

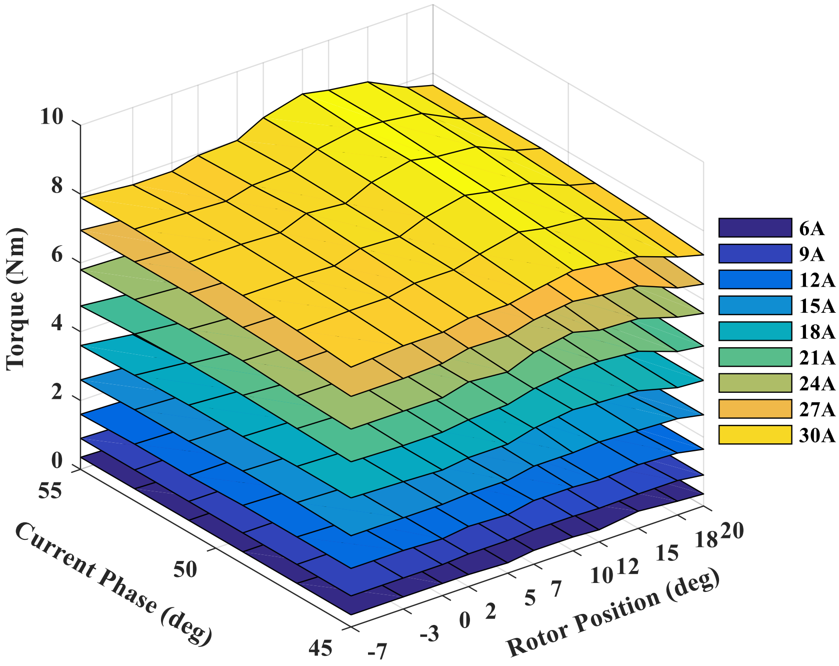

Figure 16. Measured torque vs. current phases and rotor positions.

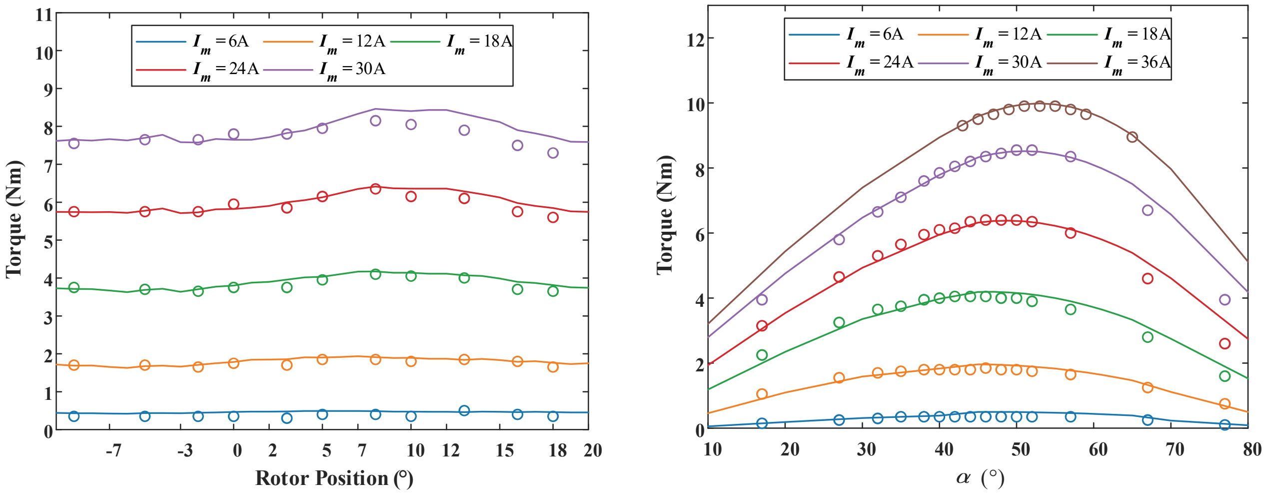

(**a**) (**b**)

Figure 17. Comparison of the measured and FEA calculated torque results: (**a**) torque values by different current and rotor position; (**b**) torque values by different current and current angle.

Table 8. Power loss and efficiency at rated operation.

Item	FEA Results
Iron loss	15.7 W
Copper loss	130.8 W
Efficiency	91.40%
Power factor	0.65
Speed	1500 r/min

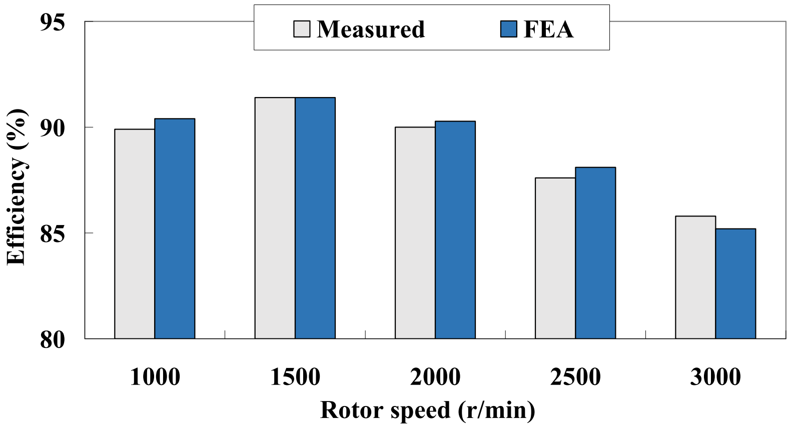

Figure 18. Comparison of the measured and FEA calculated efficiency by different rotor speed.

7. Conclusions

This paper demonstrates the electromagnetic performance of a 12/4 SynRM with concentrated windings. The non-linear MEC model of the 12/4 SynRM is built to get the air-gap flux density, coil flux-linkages, armature winding inductances, etc. The saturation effect is counted in by the MEC. The MEC model is validated by 2D-FEA. Then, the parameter optimization method based on Taguchi and MEC is proposed, aiming at the best average torque, lowest torque ripple and THD in phase voltage. Overall, the proposed Taguchi-MEC method exhibits comparable accuracy with traditional FEA-based multi-object parameter optimization methods, but using much less time. It should be emphasized that the MEC is not used to deal with complex topologies such as a rotor with a non-uniform rotor iron shape or rotor outline. Nevertheless, the proposed MEC-Taguchi method can be employed to obtain a roughly optimized topology that can be used as the initial design to be further optimized by FEA.

Author Contributions: Conceptualization, G.Z.; data curation, Y.L., G.Z. and J.T.; formal analysis, G.Z. and Z.C.; funding acquisition, Z.C. and W.H.; investigation, G.Z. and Y.L.; methodology, G.Z., X.X. and Y.L.; supervision, G.Z. and Z.C.; writing—original draft, G.Z. All authors have read and agreed to the published version of the manuscript.

Funding: This work is supported in part by the National Nature Science Foundation of China under Grant 51937006, 52077032, 51991380, in part by CALT under Grant CALT201806, in part by the Fundamental Research Funds for the Central Universities under Grant 2242021R41129, and in part by the Technology Foundation for Selected Overseas Chinese Scholar under Grant 1116000256.

Conflicts of Interest: The authors declare no conflict of interest.

References

1. Bianchi, N.; Bolognani, S.; Bon, D.; Pré, M.D. Torque harmonic compensation in a synchronous reluctance motor. *IEEE Trans. Energy Convers.* **2008**, *23*, 466–473. [CrossRef]
2. Bianchi, N.; Bolognani, S.; Bon, D.; Pre, M.D. Rotor flux-barrier design for torque ripple reduction in synchronous reluctance and PM-assisted synchronous reluctance motors. *IEEE Trans. Ind. Appl.* **2009**, *45*, 921–928. [CrossRef]
3. Lopez-Torres, C.; Bacco, G.; Bianchi, N.; Espinosa, A.G.; Romeral, L. A parallel analytical computation of synchronous reluctance machine. In Proceedings of the 2018 XIII International Conference on Electrical Machines (ICEM), Alexandroupoli, Greece, 3–6 September 2018; pp. 25–31.
4. Babetto, C.; Bacco, G.; Bianchi, N. Synchronous reluctance machine optimization for high-speed applications. *IEEE Trans. Energy Convers.* **2018**, *33*, 1266–1273. [CrossRef]
5. Murataliyev, M.; Degano, M.; Galea, M. A novel sizing approach for synchronous reluctance machines. *IEEE Trans. Ind. Electron.* **2021**, *68*, 2083–2095. [CrossRef]
6. Moghaddam, R.; Gyllensten, F. Novel high-performance synrm design method: An easy approach for a complicated rotor topology. *IEEE Trans. Ind. Electron.* **2014**, *61*, 5058–5065. [CrossRef]
7. Spargo, S.M.; Mecrow, B.C.; Widmer, J.D.; Morton, C.; Baker, N.J. Design and validation of a synchronous reluctance motor with single tooth windings. *IEEE Trans. Energy Convers.* **2015**, *30*, 795–805. [CrossRef]
8. Spargo, C.M.; Mecrow, B.C.; Widmer, J.D.; Morton, C. Application of fractional-slot concentrated windings to synchronous reluctance motors. *IEEE Trans. Ind. Appl.* **2015**, *51*, 1446–1455. [CrossRef]
9. Spargo, C.M.; Mecrow, B.C.; Widmer, J.D. Electromagnetic analysis of a synchronous reluctance motor with single-tooth windings. *IEEE Trans. Magn.* **2017**, *53*, 8206207.
10. Spargo, C.M. Electromagnetic–mechanical design of synchronous reluctance rotors with fine features. *IEEE Trans. Magn.* **2017**, *53*, 8206308.
11. Babetto, C.; Bianchi, N.; Torreggiani, A.; Bianchini, C.; Davoli, M.; Bellini, A. Optimal design and experimental validation of a synchronous reluctance machine for fault-tolerant applications. In Proceedings of the 2019 IEEE Energy Conversion Congress and Exposition (ECCE), Baltimore, MD, USA, 29 September–3 October 2019; pp. 4880–4887.
12. Lehner, B.; Gerling, D. Design considerations for concentrated winding synchronous reluctance machines. In Proceedings of the 2016 IEEE Transportation Electrification Conference and Expo, Asia-Pacific (ITEC), Busan, Korea, 1–4 June 2016; pp. 485–490.
13. Gamba, M.; Pellegrino, G.; Armando, E.; Ferrari, S. Synchronous reluctance motor with concentrated windings for IE4 efficiency. In Proceedings of the 2017 IEEE Energy Conversion Congress and Exposition (ECCE), Cincinnati, OH, USA, 1–5 October 2017; p. 17351585.
14. Ma, X.Y.; Li, G.J.; Zhu, Z.Q.; Jewell, G.W.; Green, J. Investigation on synchronous reluctance machines with different rotor topologies and winding configurations. *IET Electr. Power Appl.* **2018**, *12*, 45–53. [CrossRef]
15. Jannot, X.; Vannier, J.; Marchand, C.; Gabsi, M.; Michel, J.S.; Sadarnac, D. Multiphysic modeling of a high-speed interior permanentmagnet synchronous machine for a multiobjective optimal design. *IEEE Trans. Energy Convers.* **2011**, *26*, 457–467. [CrossRef]
16. Nakata, T.; Sanada, M.; Morimoto, S.; Inoue, Y. Automatic design of IPMSMs using a genetic algorithm combined with the coarse-mesh FEM for enlarging the high-efficiency operation area. *IEEE Trans. Ind. Electron.* **2017**, *64*, 9721–9728. [CrossRef]
17. Rostami, N.; Feyzi, M.R.; Pyrhonen, J.; Parviainen, A.; Behjat, V. Genetic algorithm approach for improved design of a variable speed axial-flux permanent-magnet synchronous generator. *IEEE Trans. Magn.* **2012**, *48*, 4860–4865. [CrossRef]
18. Ismail, M.M.; Xu, W.; Wang, X.G.; Junejo, A.K.; Liu, Y.; Dong, M.H. Analysis and optimization of torque ripple reduction strategy of surface-mounted permanent-magnet motors in flux-weakening region based on genetic algorithm. *IEEE Trans. Ind. Appl.* **2021**, *57*, 4091–4106. [CrossRef]
19. Dong, F.; Zhao, J.; Song, J.; Feng, Y.; He, Z. Optimal design of permanent magnet linear synchronous motors at multispeed based on particle swarm optimization combined with SN ratio method. *IEEE Trans. Energy Convers.* **2018**, *33*, 1943–1954. [CrossRef]

20. Lee, J.H.; Song, J.; Kim, D.; Kim, J.; Kim, Y.; Jung, S. Particle swarm optimization algorithm with intelligent particle number control for optimal design of electric machines. *IEEE Trans. Ind. Electron.* **2018**, *65*, 1791–1798. [CrossRef]
21. Lin, F.; Teng, L.; Chu, H. A robust recurrent wavelet neural network controller with improved particle swarm optimization for linear synchronous motor drive. *IEEE Trans. Power Electron.* **2008**, *23*, 3067–3078. [CrossRef]
22. Chen, Z.; Li, W.C.; Shu, X.; Shen, J.W.; Zhang, Y.J.; Shen, S.Q. Operation efficiency optimization for permanent magnet synchronous motor based on improved particle swarm optimization. *IEEE Access* **2020**, *9*, 777–788. [CrossRef]
23. Lee, S.J.; Kim, K.S.; Cho, S.; Jang, J.; Lee, T.H.; Hong, J.P. Optimal design of the magnetizing fixture using Taguchi robust design in the ringtype PMSM. In Proceedings of the 7th IET International Conference on Power Electronics, Machines and Drives (PEMD 2014), Manchester, UK, 8–10 April 2014; pp. 1–6.
24. Dong, F.; Song, J.; Zhao, J.; Zhao, J. Multi-objective design optimization for PMSLM by FITM. *IET Electric Power Appl.* **2018**, *12*, 188–194. [CrossRef]
25. Si, J.; Zhao, S.; Feng, H.; Cao, R.; Hu, Y. Multi-objective optimization of surface-mounted and interior permanent magnet synchronous motor based on Taguchi method and response surface method. *Chin. J. Elect. Eng.* **2018**, *4*, 67–73.
26. Shi, Z.; Sun, X.D.; Cai, Y.F.; Yang, Z.B. Robust design optimization of a five-phase pm hub motor for fault-tolerant operation based on Taguchi method. *IEEE Trans. Energy Convers.* **2020**, *35*, 2036–2044. [CrossRef]
27. Amrhein, M.; Krein, P.T. Magnetic equivalent circuit simulations of electrical machines for design purposes. In Proceedings of the 2007 IEEE Electric Ship Technologies Symposium, Arlington, VA, USA, 21–23 May 2007; pp. 254–260.
28. Cao, D.; Zhao, W.; Ji, J.; Ding, L.; Zheng, J. A generalized equivalent magnetic network modeling method for vehicular dual-permanent-magnet vernier machines. *IEEE Trans. Energy Convers.* **2019**, *34*, 1950–1962. [CrossRef]
29. Zhu, Z.Q.; Pang, Y.; Howe, D.; Iwasaki, S.; Deodhar, R.; Pride, A. Analysis of electromagnetic performance of flux-switching permanent-magnet machines by nonlinear adaptive lumped parameter magnetic circuit model. *IEEE Trans. Magn.* **2005**, *41*, 4277–4287. [CrossRef]
30. Alireza, S.; Mahsa, K. Optimum design of double sided linear switched reluctance motor with Taguchi method. In Proceedings of the 2019 IEEE 28th International Symposium on Industrial Electronics (ISIE) Vancouver, Vancouver, BC, Canada, 12–14 June 2019; p. 18870309.